Haptic fMRI : A Novel Five DOF Haptic Interface for Multi-Axis Motor Neuroscience Experiments

Samir Menon[1], Amaury Soviche[2], Jananan Mithrakumar[1], Alok Subbarao[1], Hari Ganti[1], and Oussama Khatib[1].

***Abstract*— We present a novel electromagnetically actuated Haptic fMRI Interface with five degrees-of-freedom (DOF), HFI-5. The interface uses two three DOF devices connected with a gimbal in a closed kinematic chain to achieve three-axis translation and two-axis rotation. To highlight the device's design, we develop a taxonomy of similar devices and demonstrate why HFI-5's design excels. We use a cross-correlation based novel analysis method to demonstrate that HFI-5 is transparent by showing that it does not affect unconstrained subject motions. This is due to its low friction (< 0.31 N) and lightweight design. Next, we show that HFI-5 can accurately track positions, velocities, and accelerations, in part due to a 7.5 kHz servo loop. Finally, we demonstrate that HFI-5 is fMRI-compatible and does not interfere with fMRI scans even while applying large torques with its electromagnetic motors.**

I. Introduction

Realizing the potential of functional magnetic resonance imaging (fMRI) for motor neuroscience requires the development of tools that enable the study of rich manipulation tasks in a controlled setting. Haptic interfaces are ideal to meet this challenge. They can recreate a variety of day-to-day motor tasks in virtual environments [1], [2], [3], [4] while allowing experimenters to precisely monitor motions and apply forces when required. Developing a functioning multi-axis haptic interface that works with high-resolution fMRI (mm, sec) [5], [6] promises to substantially expand the study of the brain's sensorimotor regions [7]. Moreover, combining haptics with fMRI also promises dramatic improvements to motor rehabilitation [8], [9], [10], [11], [12] by allowing clinicians to observe how therapy affects neural circuits in real-time. Integrating such haptics with fMRI will allow us to step beyond classical motor neuroscience experiments, which have focused on non-interactive free-space motions.

Research efforts have led to numerous haptic interfaces for fMRI. These rely on a variety of actuators such as elecro-active polymers [13], pneumatics [14], ultrasonics [12], [15], and hydraulics [16], [15]. Cables, with dynamic models to improve performance [17], are also promising. Functional interfaces include a shielded Phantom [18], [19], a wrist device [20], a pneumatic device [14], and a family of electromagnetically actuated devices [21], [22]. Present efforts are directed towards devices with more DOF, or towards achieving high-fidelity force control, natural motions [23] and uniform inertial properties across a large three-dimensional workspace.

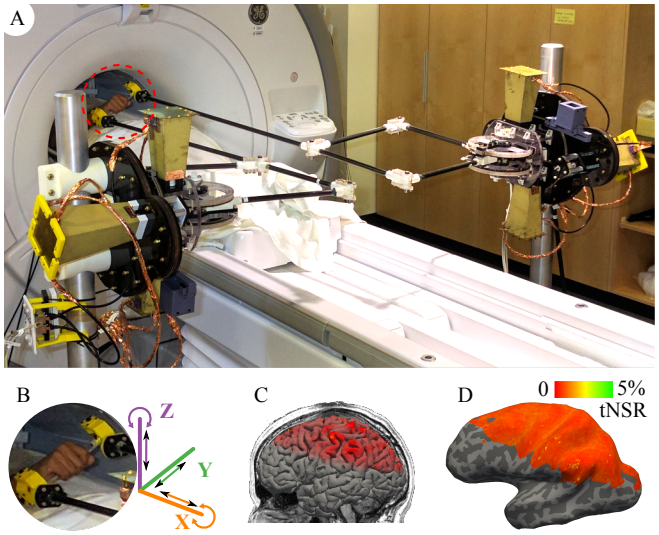

Fig. 1. Haptic fMRI Interface 5. *A*, A subject operating HFI-5 in gimbal mode inside a 3T MRI scanner. *B*, The two planar parallelograms may be moved together to realise three-axis (X, Y, Z) motions. In addition, moving them anti-parallel along the X and Z axes produces Z and X rotations respectively (see axis frame). *C*, A volumetric rendering of a human's brain demonstrates the volume spanned by an exemplar fMRI motor neuroimaging scan. *D*, Temporal noise measurements plotted on an inflated rendering of the subject's brain. fMRI recordings were made while HFI-5 applied a series of random forces and torques.

This paper presents a novel fMRI-compatible haptic interface, HFI-5, with five DOF. The device's DOF are realized using two three degree-of-freedom device modules connected in a closed-chain kinematic structure (Fig. 1). It supports translations that span the MRI workspace, as well as two-axis rotations that span the human wrist's ability to rotate. To highlight HFI-5's design advances, we present a taxonomy of possible similar devices and discuss how its design is both pragmatic and effective. We demonstrate that HFI-5 is transparent to human operators: motions performed while operating the device are indistinguishable from free space motions. Moreover, HFI-5 can accurately monitor positions, velocities, as well as accelerations due to its fast control and sensing servo loop (at ~7.5 kHz). Finally, we demonstrate that HFI-5 is fMRI-compatible and does not affect the quality

*This work was supported by BioX, Stanford University

[1]S. Menon, J. Mithrakumar, A. Subbarao, H. Ganti, and O. Khatib are with the Stanford Robotics Laboratory, Department of Computer Science, Stanford University, Stanford, CA 94305, USA. [2]A. Soviche is with the Robotics and Autonomous Systems Department, Ecole Polytechnique Fédérale de Lausanne, Route Cantonale, 1015 Lausanne, Switzerland. Email: smenon@cs.stanford.edu, janamith@stanford.edu, hganti@stanford.edu, asubbarao@stanfordhealthcare.org, ok@cs.stanford.edu, amaury.soviche@epfl.ch

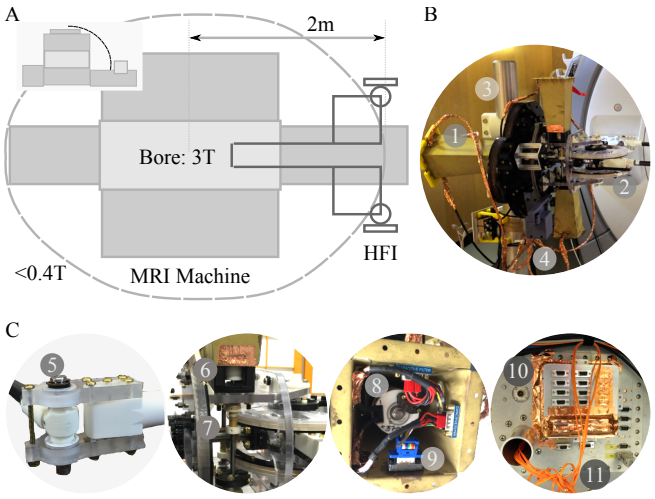

Fig. 2. HFI-5 Design. *(A)*, Dual planar parallelogram devices connected with a gimbal help realize five actuated DOF in a large and stiff kinematic structure. Electromagnetic actuators and sensors lie beyond the 0.4 Tesla (400 Gauss) magnetic field line (top view; inset shows side view). *(B)*, A view of HFI-5's device base shows: *(1)* the shielded motors, *(2)* parallelogram plane intersects the base rotation axis (not coupled), *(3)* an adjustable height assembly, and, *(4)*, an adjustable gravity compensator. *(C)*, Additional HFI-5 design features include: *(5)*, full-ceramic bearings and a stiffer pin joint; *(6)*, a stiff and compact polycarbonate base frame with accessible motors; *(7)*, a bi-directional kevlar cable drive with a low-friction teflon-coated capstan; *(8)*, capacitive filters for 48V motor wiring; *(9)*, separately insulated and grounded filters for 5V encoder wiring *(10)*, a capacitive filterbank built into the MRI-room faraday cage to filter and ground all electrical connections, and, *(11)*, optical fiber connections for (optional) optical sensors.

of fMRI measurements in the human brain, even while applying a variety of different forces.

II. Design

Designing a transparent multi-axis fMRI-compatible haptic interface that can provide high fidelity actuation over a large workspace poses numerous design and engineering challenges. Based on our past experience with Haptic fMRI (HFI-3 family [21], [22], [24], [25] and particle jamming interfaces [26]), we chose to prioritize the following in rank-order: *(i)* no interference with fMRI measurements; *(ii)* robust operation in the MRI machine's magnetic field; *(iii)* haptic transparency; *(iv)* high fidelity force generation; *(v)* high reliability; *(vi)* ease of assembly at MRI ($<$ 20min); *(vii)* minimal cost.

The space of potential Haptic fMRI Interface designs is large, including a variety of serial and parallel devices of different sizes and DOF. A fundamental feature to classify them—one which greatly influences all other design aspects—is the type of actuator used. We decided to focus on devices that use electromagnetic actuators since such devices are robust, simplify control, and reliably provide high fidelity forces. A disadvantage, however, is that they require that the motors be carefully shielded and distanced from the MRI bore. A suitable closed-chain kinematic structure can help realize this for multi-axis control.

A. Closed-Chain Kinematics for Five-Axis Control

We realized five actuated DOF in HFI-5 using a pair of three degree-of-freedom haptic interface modules that are

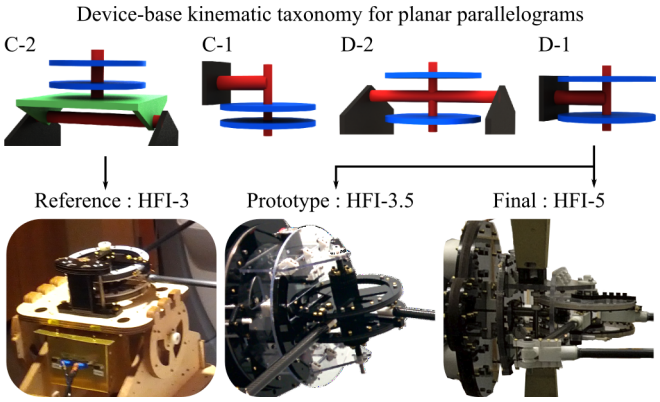

Fig. 3. Taxonomy of Planar Parallelogram Bases. *Top*, Device-base classes: *C-class* devices, have coupled dynamics between the parallelogram and the third rotational axis (due to a position offset). *D-class* devices, in contrast, decouple parallelogram motion and base axis rotation. A 1 or 2 numeric value indicates the number of supports for the base's rotation axis. *Bottom*, A *C-2* device (HFI-3) developed earlier serves as a reference for HFI-5. We designed and fabricated two *D-1* devices: a prototype, HFI-3.5, and the final interface, HFI-5.

connected with a gimbal at their end-effector (see Fig. 1). Each haptic interface module uses a planar parallelogram to distance the actuator assembly from the MRI-bore and remotely project the DOF. Two motors actuate the parallelogram (Maxon 148877) itself and another motor (Maxon 370356) rotates the base, providing each module with three DOF. While the resulting composite device has six actuators, the end-effector connection imposes a constraint and leads to the loss of a rotational degree-of-freedom along the axis of the connecting gimbal (see Fig. 1.B). As a consequence, the composite device has five DOF: translations and force control along x, y, and z, along with rotations and torque control along x, and z (see Table II for workspace).

HFI-5's design adopts the HFI-3 family's planar parallelogram for its left and right modules (Fig. 2). HFI-5's planar parallelogram, however, is a dramatic improvement over HFI-3's parallellogram (see Fig. 2.B,C). It is height adjustable, is much stiffer, and benefits from an improved pin-joint design. Moreover, the parallelogram assembly can easily be detached from the base, disassembled, and reassembled. A bi-directional cable drive ensures that the drivetrain does not slip. It also allows an operator to control cable-tension induced friction independently for the clockwise and counter-clockwise directions.

The HFI-5 gimbal also presents some design challenges since it has a major impact on the overall friction and perceived transparency. In addition, it is best to construct it entirely out of non-metallic materials. Finally, it must be easy to attach and detach: a requirement to disassemble the device for transporting to and from the robotics workshop. We realized a lightweight and very low friction design (see Fig. 1.B) using custom manufactured ceramic bearings (ABEC-3; C2; ZrO2 balls and race; PTFE cage), a polystyrene and acrylic structure, and glass-filled nylon screws and nuts.

We briefly note that HFI-5 can operate in a bi-manual mode without the gimbal. In this mode, it provides three translation DOF at each hand.

B. Device-Bases that Minimize Kinematic Coupling

To select a suitable device-base design, we began by identifying a taxonomy of device-bases for planar parallelogram devices (Fig. 3). Our taxonomy includes four broad classes of device-bases, which are delineated from each other based on: *(i)* whether they couple the dynamics of the planar parallelogram with the base rotation (C-class) or not (D-class); and, *(ii)*, whether they support the base at two points (type 2), or require a cantilever design with a single support point (type 1).

D-2 devices present an ideal. They minimize coupling and provide a very stable foundation, which maximizes stiffness at the end-effector. Such devices, unfortunately, are complex to design, potentially bulky, hard to transport and assemble, and have a tendency to induce anisotropic force and inertial properties at the end-effector. The opposite of D-2 devices, C-1 devices, perform poorly in every regard. C-2 and D-1 devices are practical and worth investigating.

Having empirically investigated both C-2 and D-1 devices (see Fig. 3), we decided to construct HFI-5 using D-1 bases for its left and right modules. Its decoupled parallelogram dynamics offer a substantial and palpable increase in device stiffness and transparency, particularly along the up-down motion axis. It greatly simplifies access to the motors and the drivetrain, which makes maintenance easy. Another advantage of segregating motors is that the wiring, which carries analog signals over about 5m of cable, is decoupled as well. Finally, the contribution of the motors to the base axis inertia is symmetric.

Moving to HFI-5's design-class independent improvements, we first note that its capstans have an adjustable gear ratio, which allows users to customize the trade-off between peak force and reflected end-effector inertia. Next, the polycarbonate body is reinforced and designed to greatly increase stiffness; albeit at the expense of marginally increasing inertia. The body also has an adjustable passive gravity compensator, which allows making the end-effector almost weightless across the entire MRI-workspace. For a more detailed discussion about actuators, materials, inertias, forces, and condition numbers, which are broadly shared with HFI-3, kindly see [21]. Device metrics are enumerated in Table II.

III. Haptic Transparency

We tested HFI-5's transparency with a series of tests comparing subject motions in free space to those while holding the haptic interface (Fig. 4). Subjects were requested to repeatedly draw a triangle and a U-like shape over a time-period of a few minutes while lying supine (mimicking the MRI posture; all triangles and then all Us). Motions were entirely decided by the subject. We did not provide any feedback apart from instructing them, in advance, to attempt to be reliable and consistent. Motions in free space were tracked with optical motion capture markers attached to the end of a light (100g) carbon fiber rod (see Appendix for details).

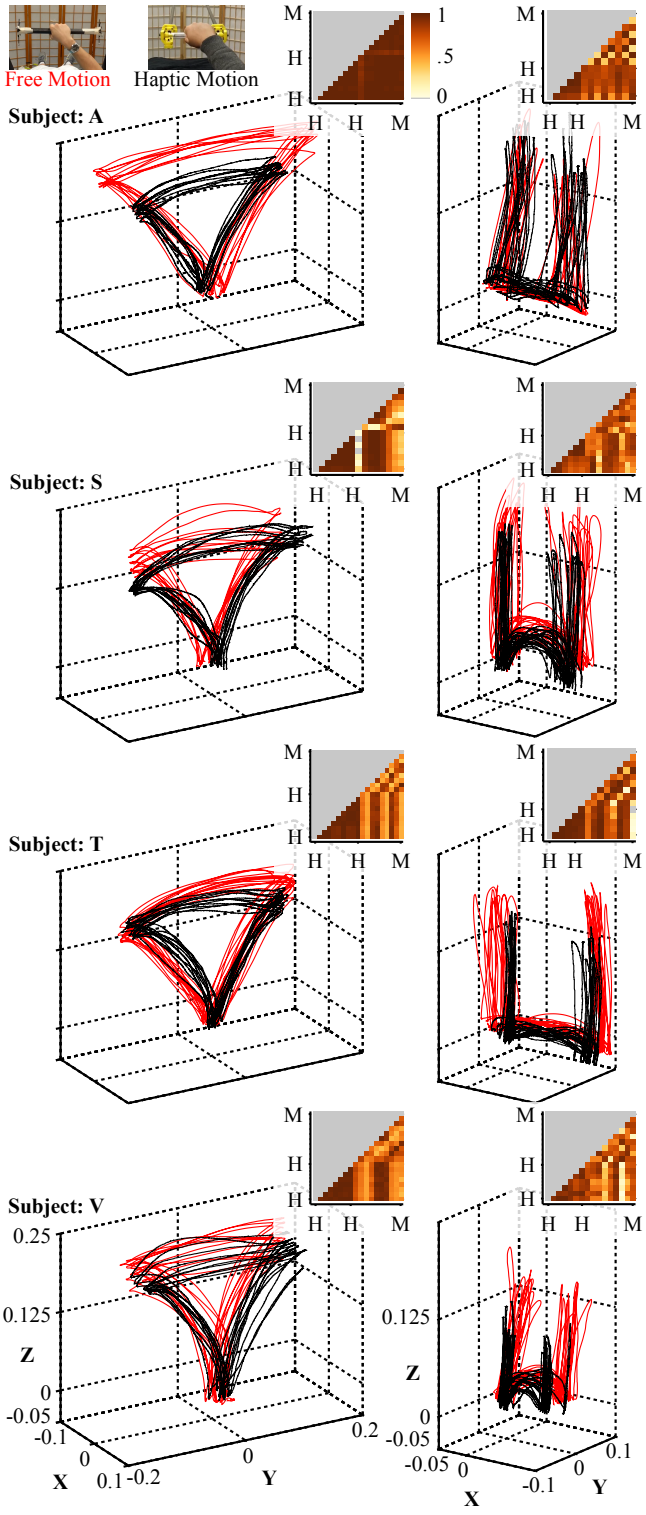

Fig. 4. HFI-5 Transparency. Unconstrained motions captured while subjects moved in free space while holding a carbon-fiber rod (red) match motions with HFI-5 (black). Four subjects drew multiple triangles or U-shapes. Inset figures show the cross-correlation matrices for haptic and motion trajectories across all repetitions: y-axis for triangles, and z-axis for U-shapes.

We computed the cross-correlation of each drawing instance with every other instance, which allowed us to estimate the degree of reliability in unconstrained motions as well as the degree to which HFI-5 interfered with natural

TABLE I

HAPTIC TRANSPARENCY CROSS-CORRELATION

Trial-Type	A	S	T	V
$\Delta_{h-y}(0.5\%ile)$	0.988	0.971	0.948	0.966
$\Delta_{h-y}(99.5\%ile)$	0.995	0.996	0.991	0.992
$\Delta_{h-z}(0.5\%ile)$	0.937	0.963	0.984	0.978
$\Delta_{h-z}(99.5\%ile)$	0.988	0.988	0.994	0.994
$U_{h-x}(0.5\%ile)$	0.914	0.960	0.963	0.971
$U_{h-x}(99.5\%ile)$	0.972	0.988	0.998	0.993
$U_{h-z}(0.5\%ile)$	0.934	0.944	0.966	0.921
$U_{h-z}(99.5\%ile)$	0.986	0.987	0.992	0.978
$\Delta_{m-y}(0.5\%ile)$	0.977	0.917	0.909	0.939
$\Delta_{m-y}(99.5\%ile)$	0.992	0.992	0.992	0.990
$\Delta_{m-z}(0.5\%ile)$	0.921	0.920	0.902	0.927
$\Delta_{m-z}(99.5\%ile)$	0.976	0.978	0.971	0.968
$U_{m-x}(0.5\%ile)$	0.951	0.912	0.911	0.953
$U_{m-x}(99.5\%ile)$	0.985	0.936	0.992	0.992
$U_{m-z}(0.5\%ile)$	0.932	0.925	0.915	0.905
$U_{m-z}(99.5\%ile)$	0.990	0.949	0.962	0.959
$\Delta_{h-m-y}(0.5\%ile)$	0.988	0.924	0.917	0.934
$\Delta_{h-m-y}(99.5\%ile)$	0.993	0.992	0.983	0.971
$\Delta_{h-m-z}(0.5\%ile)$	0.925	0.942	0.919	0.921
$\Delta_{h-m-z}(99.5\%ile)$	0.983	0.990	0.989	0.988
$U_{h-m-x}(0.5\%ile)$	0.913	0.907	0.916	0.964
$U_{h-m-x}(99.5\%ile)$	0.965	0.969	1.000	0.993
$U_{h-m-z}(0.5\%ile)$	0.917	0.903	0.941	0.905
$U_{h-m-z}(99.5\%ile)$	0.983	0.987	0.967	0.962

motions. Since motions were unconstrained and there was no limit on the time taken, there was significant variation across trials in both spatial shape and time taken. We manually segmented recorded trajectories into individual trials. We then corrected for timing offsets by first computing the cross-correlations for any two given trajectories for a ±0.2s offset, and time-shifting one so their cross-correlation was maximized. This also corrected for timing offsets between different repetitions. To study motions independently across axes, we computed correlations individually for the relevant motion axes. Data was downsampled to 100Hz to simplify plotting. The x- and y-axes were irrelevant for the triangle and U-shape, respectively.

The cross-correlation of individual drawing instances was high and consistent for all subjects while using HFI-5 (see Fig. 4, insets). The cross-correlation was high but less consistent while moving in free space (see Fig. 4, insets). The cross-correlation between haptic and free motions was similar, which indicates that HFI-5 is transparent. Bootstrap 99% confidence intervals of the trial-to-trial cross-correlation for the triangle (Δ) and U motions can be found in Table I. Most confidence intervals overlap indicating that that haptic-to-haptic (h) and mocap-to-mocap (m) motions have a similar distribution as the haptic-to-mocap (h-m) motions. Minor differences in the trajectory cross correlation values may be attributed to the lack of any feedback and entirely unstructured experimental setup.

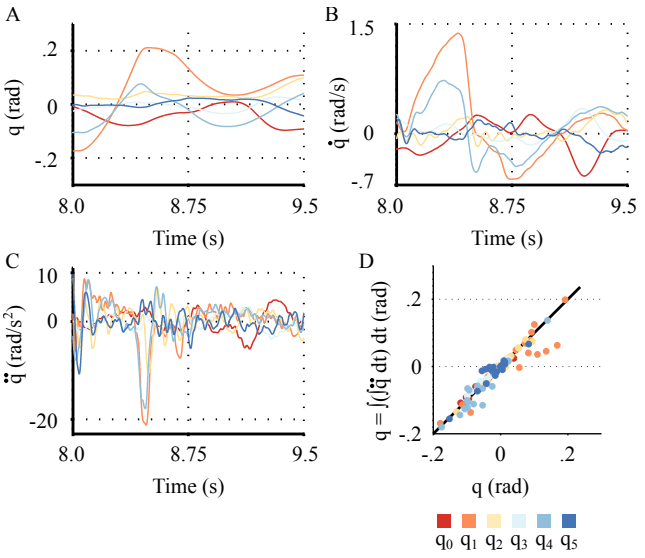

Fig. 5. HFI-5 Trajectory Tracking. Exemplar snippets (1.5s) of joint position (*A*), velocity (*B*), and acceleration (*C*) recorded at 7450Hz. Trajectories are part of a longer (28s) recorded human motion. (*D*), A scatter plot of double integrated acceleration against position demonstrates that accelerations for most joints are estimated accurately.

IV. HFI-5: MOTION TRACKING

We tested HFI-5's ability to accurately estimate positions, velocities, and accelerations by analyzing motion data while a human operated it (Fig. 5). The high control rate (~7.5 kHz; Sensoray 826 IO board, Copley current control 4122 amplifiers) and high resolution encoders (US Digital, 10,000 CPR, 4x quadrature) allow accurately estimating accelerations. We tested the fidelity of the acceleration estimates by double integrating them using a forward Euler integrator. The integrated positions so obtained closely matched the actual positions (see Fig. 5.D) for all but one joint. The estimates may be improved further using a dynamic model of the robot. They may also be improved by modeling and compensating for device deflection during high accelerations such as those plotted.

V. fMRI COMPATIBILITY: NOISE TESTS

We tested HFI-5's fMRI compatibility with three human fMRI experiments. First, we placed the device in the scanner but left it inactive. We then performed an fMRI scan (see Appendix for scanning details) of a human subject who lay passive in the MRI bore. Having done so, we proceeded to conduct two systematic tests of HFI-5's force generation capability. The first applied a series of sine wave torques, while the second applied a series of ramp and hold torques. An operator fixed HFI-5 in place during the force trials. Concurrent with the forces, we conducted two fMRI scans and determined temporal noise introduced in the fMRI measurements during HFI-5's operation (Fig. 6).

With the first force experiment, we tested whether HFI-5 affected the temporal noise of fMRI measurements during the application of a series of sine waves to one or more actuators. We first applied a 1Hz sine wave torque (peak-to-peak 3 Nm) at the zeroth actuator (up-down force) of the left

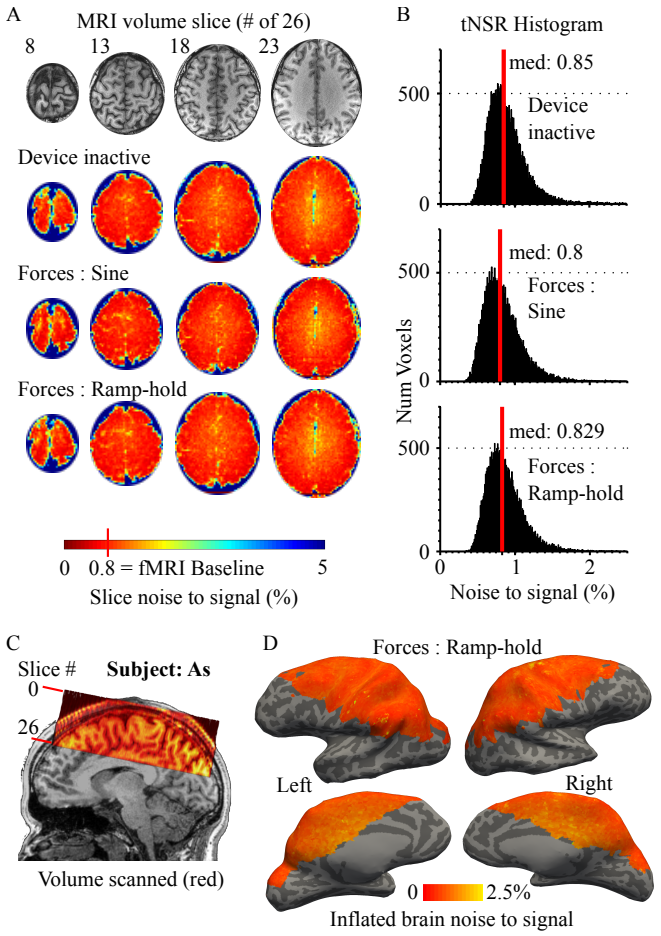

Fig. 6. HFI-5 fMRI Noise Tests. Temporal noise for fMRI scans of motor, parietal, and parts of visual cortex taken while HFI-5 was ether inactive or applying forces. (*A*). Exemplar fMRI slices along with a temporal noise heatmap at each voxel for different HFI-5 tests. (*B*). Temporal noise histograms show the noise-to-signal distribution across all brain voxels. (*C*). The fMRI scan area relative the subjects' brain, with slice indices. (*D*). Invididual voxel temporal noise mapped to a subject-specific inflated-brain model.

module. Next we applied the same torque to the right module, and then to both. We then repeated the same pattern for the first (MRI-bore axial force) and second (left-right force) of the left and right modules. This pattern repeated for a total test time of about four minutes.

With the second force experiment, we tested HFI-5 by applying a series of ramp-hold-zero sequences to the different motors. We first ramped up torques at the zeroth motor of the left module (to 3 Nm at 1 Nm/s), held the peak torque for 2s, and returned to zero. Next, we repeated the pattern for the right module zeroth motor. We then repeated the pattern for the first and second motor pairs of the left and right modules. Next, we applied the pattern simultaneously to all motors on the left module, and then on the right module. Finally, we applied the pattern to all motors across both modules. The pattern repeated for about five and a half minutes.

We then computed temporal noise (see Appendix for details) for each human experiment and plotted it as a heatmap over fMRI slices as well as over the inflated brain surface (see Fig. 6.A,D). The temporal noise histograms for

TABLE II
HAPTIC DEVICE METRICS

Metric	Desired	HFI-5
Position error	$<$1 *mm* [1], [3]	~.001, .02, .025 *mm (x,y,z)*
End-effector force	~5 *N*	16.36, 4.62, 6.90 *N (x,y,z)*
End-effector friction	minimal	.31, .17, .13 *N (x,y,z)*
Force condition no.	1	3.54
Control update rate	$>$350 *Hz* [1]	$>$7,450 *Hz*
Workspace	~.65x.40x.20 m^3	$>$.5x1.00x1.4 m^3
Temporal Noise	$<$ 2% [27]	$<$ 1%

our fMRI data were indistinguishable across experiments whether the device was off or applying forces (see Fig. 6.B). Minor differences in the noise median are consistent with fMRI variability observed across other Haptic fMRI noise measurements with respect to expected baseline noise (see [21], [22] for more details).

VI. CONCLUSIONS AND DISCUSSION

To summarize, we present a novel fMRI-compatible haptic interface, HFI-5, with five DOF. This device, the first of its kind, greatly improves upon previous Haptic fMRI devices, is transparent to human subjects, and does not interfere with human fMRI scans. HFI-5 presents a landmark for Haptic fMRI since it finally enables complex multi-axis motor neuroscience experiments. We foresee future research using this device to characterize how the brain achieves motor control and tactile perception for manipulation tasks. We also foresee a six degree-of-freedom haptic interface for fMRI, which will represent the culmination of this technical program.

APPENDIX

fMRI Scanning: All fMRI scans were conducted at Stanford University's Center for Cognitive and Neurobiological Imaging on a GE Discovery MR750 3 Tesla MRI scanner, with a 32 channel Nova Medical head coil. The scan protocol was gradient echo EPI with a 16cm field of view sampled at a 64x64 resolution (2.5x2.5x2.5 mm^3 voxels), a 1.57s repetition time, a 28ms echo time, and a 72^o flip angle. All scan runs were preceeded by 2^{nd}-order polynomial shimming and were sandwiched by fieldmap scans. After scanning, the fMRI images were slice time corrected, motion corrected (SPM), spatially undistorted using fieldmaps, and analyzed to compute temporal signal-to-noise. A subject-customized bite-bar minimized head motion.

Haptic Data: Motions were right handed. The haptic control loop was ~7450Hz. As part of the haptic control interface, haptic trajectories were filtered with a second order Savitzky-Golay filter (programmed in C++) to remove high frequency noise and estimate derivatives.

Human Subjects: Subjects were healthy right-handed males with no history of motor disorders: As, 26yr, 148lb, 5'7"; A, 23yr, 166lb, 6'0"; S, 32yr, 185lb, 5'9"; T, 21yr, 115lb, 5'6"; V, 22yr, 115lb, 5'7". Informed consent was obtained in advance on a protocol approved by the Institutional Review Board (IRB) at Stanford University.

Motion Capture: Motions were right handed. A Vicon Blade optical marker tracking system captured natural-motion and haptic-use trajectories. Subjects were asked to hold a tube of the same diameter as the HFI-5 handle. One optical marker was placed on each end of the tube. Markers were monitored at 240Hz.

ACKNOWLEDGMENTS

We acknowledge Jihee Hwang, Fahad Al-Shaibani, Deeksha Goyal, Valerie Hau, and Sahaana Suri, for their assistance in constructing and calibrating the electrical control system for HFI-5. Jack Zhu helped designing HFI-5's stand, and helped construct the prototype D-1 device. Takatoki Migimatsu and Vikranth Reddy assisted with optical motion capture. Kendrick Kay, Laima Baltusis, and Robert Dougherty helped develop fMRI protocols. This work was supported by National Science Foundation National Robotics Initiative grant (IIS-1427396, O. Khatib and R. Bajcsy), and by a Stanford Center for Neurobiological Imaging Seed Grant (S. Menon).

REFERENCES

[1] K. S. Hale and K. M. Stanney, "Deriving haptic design guidelines from human physiological, psychophysical, and neurological foundations," *Computer Graphics and Applications, IEEE*, vol. 24, no. 2, pp. 33 –39, March-April 2004.

[2] J. K. Salisbury, F. Conti, and F. Barbagli, "Haptic rendering: Introductory concepts," *IEEE Computer Graphics and Applications*, vol. 24, no. 2, pp. 24–32, March 2004.

[3] F. Conti and O. Khatib, "Spanning large workspaces using small haptic devices," *Proc. of the Eurohaptics on Haptic Interfaces for Virtual Environment and Teleoperator Systems*, pp. 183–188, Mar. 2005.

[4] ——, "A new actuation approach for haptic interface design," *The International Journal of Robotics Research*, vol. 28, no. 6, pp. 834–848, 2009.

[5] N. K. Logothetis, "What we can do and what we cannot do with fmri," *Nature*, vol. 453, no. 7197, pp. 869–878, Jun 2008.

[6] J. D. Meier, T. N. Aflalo, S. Kastner, and M. S. A. Graziano, "Complex organization of human primary motor cortex: A high-resolution fMRI study," *Journal of Neurophysiology*, vol. 100, pp. 1800–1812, 2008.

[7] R. Shadmehr, M. A. Smith, and J. W. Krakauer, "Error correction, sensory prediction, and adaptation in motor control," *Annual Review of Neuroscience*, vol. 33, no. 1, pp. 89–108, 2010.

[8] H. Sveistrup, "Motor rehabilitation using virtual reality," *Journal of NeuroEngineering and Rehabilitation*, vol. 1, no. 1, p. 10, 2004.

[9] J. Broeren, M. Rydmark, A. Bjrkdahl, and K. S. Sunnerhagen, "Assessment and training in a 3-dimensional virtual environment with haptics: A report on 5 cases of motor rehabilitation in the chronic stage after stroke," *Neurorehabilitation and Neural Repair*, vol. 21, no. 2, pp. 180–189, March-April 2007.

[10] J. W. Krakauer, "Motor learning: its relevance to stroke recovery and neurorehabilitation," *Current opinion in neurology*, vol. 19, no. 1, pp. 84–90, 2006.

[11] S. R. Zeiler and J. W. Krakauer, "The interaction between training and plasticity in the post-stroke brain," *Current opinion in neurology*, vol. 26, no. 6, p. 609, 2013.

[12] A. U. Pehlivan, F. Sergi, A. Erwin, N. Yozbatiran, G. E. Francisco, and M. K. O'Malley, "Design and validation of the ricewrist-s exoskeleton for robotic rehabilitation after incomplete spinal cord injury," *Robotica*, vol. 32, no. 08, pp. 1415–1431, 2014.

[13] J. Vogan, A. Wingert, J. Plante, S. Dubowsky, M. Hafez, and D. Kacher, "Manipulation in mri devices using electrostrictive polymer actuators: with an application to reconfigurable imaging coils," in *IEEE International Conference on Robotics and Automation*, 2004, pp. 2498–2504.

[14] J. Diedrichsen, Y. Hashambhoy, T. Rane, and R. Shadmehr, "Neural correlates of reach errors," *The Journal of Neuroscience*, vol. 25, no. 43, pp. 9919–9931, 2005.

[15] S. Klare, A. Peer, and M. Buss, "Development of a 3 dof mr-compatible haptic interface for pointing and reaching movements," *Lecture Notes in Computer Science*, vol. 6192, pp. 211–218, 2010.

[16] E. Burdet, R. Gassert, G. Gowrishankar, and H. Bleuler, "fmri compatible haptic interfaces to investigate human motor control," *Experimental Robotics IX*, vol. 21, pp. 25–34, 2006.

[17] D. Chapuis, R. Gassert, G. Gowrishankar, E. Burdet, and H. Bleuler, "Investigation of a cable transmission for the actuation of mr compatible haptic interfaces," in *Proc. of Biomedical Robotics and Biomechatronics*, 2006, pp. 426–431.

[18] A. Hribar, B. Koritnik, and M. Munih, "Phantom haptic device upgrade for use in fmri," *Medical and Biological Engineering and Computing*, vol. 47, pp. 677–684, 2009.

[19] T. Massie and J. Salisbury, "The phantom haptic interface: A device for probing virtual objects," in *Proceedings of the ASME winter annual meeting, symposium on haptic interfaces for virtual environment and teleoperator systems*, vol. 55-1. IOS Press, 1994, pp. 295–300.

[20] A. Erwin, M. O'Malley, D. Ress, and F. Sergi, "Kinesthetic feedback during 2dof wrist movements via a novel mr-compatible robot," *IEEE Transactions on Neural Systems and Rehabilitation Engineering*, 2016.

[21] S. Menon, G. Brantner, C. Aholt, K. Kay, and O. Khatib, "Haptic fMRI : Combining functional neuroimaging with haptics for studying the brain's motor control representation," in *Proceedings of the 13th Annual Conference of the IEEE Engineering in Medicine and Biology Society*, July 2013, pp. 4137–42.

[22] S. Menon, H. Ganti, and O. Khatib, "Using haptic fmri to enable interactive motor neuroimaging experiments," *Springer Tracts in Experimental Robotics*, vol. 81, 2014.

[23] M. Kostic, D. Popovic, and M. Popovic, "Influence of planar manipulandum to the hand trajectory during point to point movement," in *IEEE International Conference on Rehabilitation Robotics*, July 2011, pp. 1–4.

[24] S. Menon, M. Yu, K. Kay, and O. Khatib, "Haptic fMRI : Accurately estimating neural responses in motor, pre-motor, and somatosensory cortex during complex motor tasks," in *Proceedings of the 14th Annual Conference of the IEEE Engineering in Medicine and Biology Society*, August 2014.

[25] S. Menon, P. Quigley, M. Yu, and O. Khatib, "Haptic fMRI : Using classification to quantify task-correlated noise during goal-directed reaching motions," in *Proceedings of the 14th Annual Conference of the IEEE Engineering in Medicine and Biology Society*, August 2014.

[26] S. Menon, A. Stanley, J. Zhu, A. Okamura, and O. Khatib, "Mapping stiffness perception in the brain with an fMRI-compatible particle-jamming haptic interface," in *Proceedings of the 14th Annual Conference of the IEEE Engineering in Medicine and Biology Society*, August 2014.

[27] K. Murphy, J. Bodurka, and P. A. Bandettini, "How long to scan? the relationship between fmri temporal signal to noise ratio and necessary scan duration," *NeuroImage*, vol. 34, no. 2, pp. 565 – 574, 2007.